ChemComm

COMMUNICATION

View Article Online
View Journal

Check for updates

Cite this: DOI: 10.1039/d6cc01259k

Received 9th March 2026,
Accepted 1st April 2026

DOI: 10.1039/d6cc01259k

rsc.li/chemcomm

Lewis acidic boron–oxygen interactions activate cobalt oxysulfide for oxygen evolution reaction

Abhirami V. Krishnan, †[a] Aruna Narayanan Nair,†[a] Charles Matlock,[b] Kavish Saini,[a] Sisheed Sivaraman, [a] Deepesh Gopalakrishnan,[a] Ning Zhang [b] and Sreeprasad T. Sreenivasan *[a]

Lewis-acidic boron incorporation into amorphous cobalt oxysulfide induces charge redistribution and cooperative OH^- adsorption, enabling enhanced OER activity (10 mA cm^{-2} at 189 mV in 1.0 M KOH) with stable cycling, driven by Fermi-level electronic modulation.

Controlling adsorption energetics at the catalyst-electrolyte interface is central to improving the sluggish kinetics of the oxygen evolution reaction (OER).[1,2] At the catalyst surface, these energies are governed by metal–ligand covalency and interfacial charge distribution, so tuning local coordination is key to optimizing intermediate binding energies.[3,4] In crystalline oxides, periodic symmetry restricts the accessible local coordination motifs, limiting the fine-tuning of metal–ligand covalency and interfacial charge distribution.[5,6] Amorphous catalysts circumvent this constraint by providing diverse, non-equivalent local environments and structural flexibility.[7–9] However, this heterogeneity complicates the rational control of intermediate binding energetics, particularly in the initial OH^- adsorption/surface hydroxylation.[10,11] Among the diverse amorphous OER catalysts under active investigation, mixed-anion cobalt oxysulfides (CoO_xS_y) are attractive amorphous OER platforms because Co–S coordination can support electronic transport while Co–O bonding tunes covalency and electron density at cobalt centers.[12–15] The coexistence of O and S creates non-equivalent Co–(O, S) motifs, broadening the distribution of adsorption sites and intermediate binding energetics.[16,17] However, intrinsic mixed-anion flexibility alone may not provide sufficient control over adsorption strength and charge-transfer kinetics.[18–20] Heteroatom incorporation is widely used to further tune the electronic structure of disordered transition-metal (oxy)chalcogenides by perturbing local coordination and redistributing charge density.[21–23] Boron is particularly attractive because its electron deficiency (Lewis acidity) favors strong B–O interactions that can polarize neighboring metal-oxygen motifs, modulate metal–ligand covalency, and perturb near-Fermi-level electronic structure.[24,25] Furthermore, its small size facilitates homogeneous incorporation without obvious phase segregation.[26,27] In CoO_xS_y, such dopant-induced effects can be amplified by local bonding heterogeneity and can introduce additional adsorption motifs alongside Co centers. However, despite extensive activity reports, a mechanistic understanding that links anion/dopant chemistry to adsorption energetics in anion-mixed catalysts remains comparatively limited.

Here, we show that incorporating boron into an amorphous CoO_xS_y markedly enhances alkaline OER performance. The boron-doped catalyst (B-CoO_xS_y) reaches 10 mA cm^{-2} at an overpotential of 189 mV in 1.0 M KOH (*vs.* 290 mV for CoO_xS_y), with reduced charge-transfer resistance and stable cycling. Correlated spectroscopy and density functional theory (DFT) indicate that boron forms B–O interactions that redistribute charge, strengthen Co–O covalency, and introduce secondary OH^- adsorption motifs that cooperate with Co sites during initial surface hydroxylation at the disordered interface. Overall, this study provides a structure-electronic-activity correlation and highlights the incorporation of Lewis-acidic heteroatoms as a practical route to tune amorphous mixed-anion OER catalysts.

Following the synthesis (Fig. 1a), the structure, composition, and electronic states of CoO_xS_y and B–CoO_xS_y were characterized. X-ray diffraction (XRD) patterns of CoO_xS_y and B–CoO_xS_y display broad, diffuse features without sharp Bragg reflections, consistent with predominantly amorphous structures (Fig. S1).[28,29] Scanning Electron Microscopy (SEM) image of the pristine CoO_xS_y sample (Fig. S2) shows a hierarchical morphology, and the corresponding Energy-Dispersive X-ray spectroscopy (EDS) maps confirm the presence of Co, O, and S (Fig. S3). For the B-doped CoO_xS_y sample, SEM reveals hierarchical, rough-surfaced particles assembled from nanoscale subunits (Fig. 1b). Elemental mapping demonstrates a homogeneous distribution of Co, O, S, and B throughout the particles, indicating successful boron incorporation without

[a] *Department of Chemistry and Biochemistry, The University of Texas at El Paso, El Paso, Texas, 79968, USA. E-mail: sreenivasan@utep.edu*
[b] *Mechanical Engineering, Baylor University, Waco, TX, 76706, USA*
† These authors contributed equally to this work.

Open Access Article. Published on 01 April 2026. Downloaded on 4/22/2026 1:27:01 PM.
This article is licensed under a Creative Commons Attribution-NonCommercial 3.0 Unported Licence.

Open Access Article. Published on 01 April 2026. Downloaded on 4/22/2026 1:27:01 PM.
This article is licensed under a Creative Commons Attribution-NonCommercial 3.0 Unported Licence.

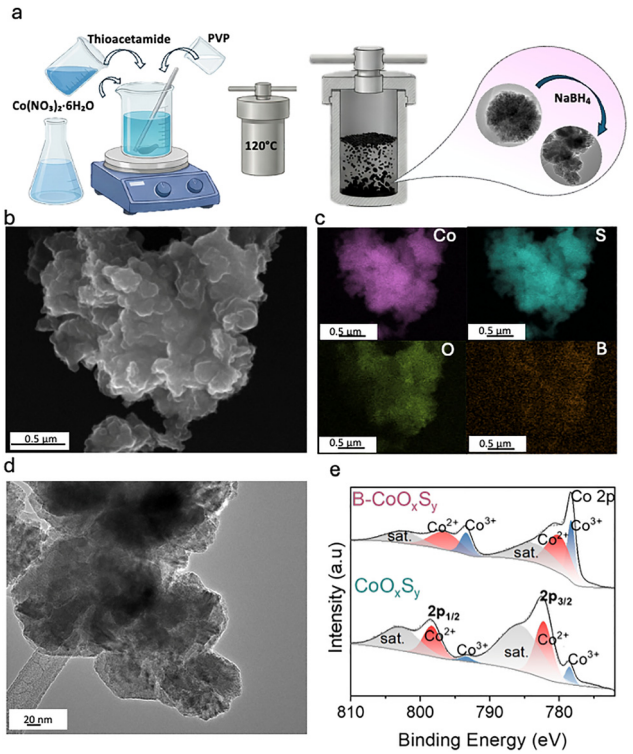

Fig. 1 (a) Schematic of the synthesis of CoO_xS_y and boron incorporation; SEM and EDS elemental maps (b) and (c) for Co, S, O and B in B–CoO_xS_y; (d) Corresponding HRTEM images of B–CoO_xS_y; (e) Peak-fitted XPS spectra of the Co 2p for B–CoO_xS_y.

observable phase segregation (Fig. 1c). Transmission electron microscopy (TEM) further shows aggregated, disordered particles, and high-resolution TEM (HR-TEM) exhibits no discernible lattice fringes for either sample, corroborating the amorphous character (Fig. 1d and Fig. S4).[29] Taken together with the amorphous XRD/HRTEM and uniform elemental mapping, these results support boron incorporation without phase segregation.

X-ray photoelectron spectroscopy (XPS) was used to probe B-induced changes in chemical state. The Co 2p spectrum of CoO_xS_y contains components consistent with cobalt in mixed sulfide/oxide coordination environments (Fig. 1e). Upon boron incorporation, the Co $2p_{3/2}$ envelope shifts to lower binding energy, indicating increased electron density at Co centers and charge redistribution within the Co–O–S network (Table S1).[12,30] The corresponding S 2p and O 1s peak deconvolutions and the elemental composition are provided in SI (Fig. S5, S6 and Table S2). The S 2p spectrum exhibits lattice sulfide features together with a higher-binding-energy contribution assigned to oxidized sulfur species.[31–33] In the doped sample, the B 1s exhibits components at ~188.9 eV and ~185.0 eV, assignable to B–O and B-metal environments (Fig. S7).[34] XPS survey quantification indicates a surface boron content of ~11.92 at% in B–CoO_xS_y (Table S2). Also, the local structures of the CoO_xS_y and B-doped CoO_xS_y were investigated by Raman spectroscopy (Fig. S8). Upon boron incorporation, these bands broaden and shift slightly, indicating modulation of the local

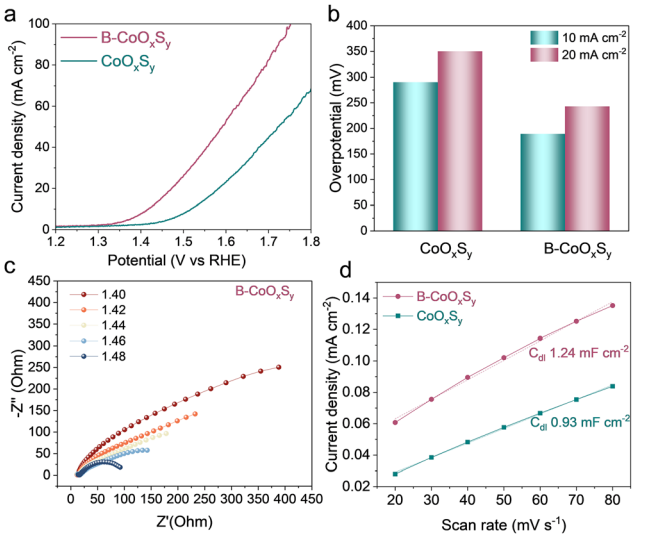

Fig. 2 (a) OER polarization curves for CoO_xS_y and B–CoO_xS_y. (b) Comparison of overpotentials at 10 and 20 mA cm^{-2}. (c) Nyquist plots of B–CoO_xS_y at the indicated potentials (*vs.* RHE). (d) C_{dl} extracted from non-faradaic CVs for ECSA comparison.

Co–O/Co–S coordination environment and increased structural disorder without the formation of secondary crystalline phases.[13,35]

After understanding the structure and chemical identity of the catalysts, the electrocatalytic OER activity was evaluated in 1.0 M KOH using a three-electrode configuration (see SI for details). Linear sweep voltammetry (LSV) polarization curves were recorded at 5 mV s^{-1} to minimize capacitive contributions. As shown in Fig. 2a, the B–CoO_xS_y exhibits an earlier onset and higher current density than CoO_xS_y. At 10 mA cm^{-2}, B–CoO_xS_y requires an overpotential of 189 mV, substantially lower than CoO_xS_y (290 mV) (Fig. 2b). Tafel analysis further supports faster OER kinetics for B–CoO_xS_y compared with CoO_xS_y (Fig. S9), consistent with modified interfacial kinetics.

Electrochemical impedance spectroscopy (EIS) was performed at OER-relevant potentials (1.40–1.48 V *vs.* the reversible hydrogen electrode, RHE) to probe interfacial charge-transfer kinetics. The Nyquist semicircle for B–CoO_xS_y decreases systematically with increasing potential (Fig. 2c), indicating reduced charge-transfer resistance (R_{ct}) under anodic polarization. The corresponding EIS spectra for CoO_xS_y are provided in Fig. S10. The electrochemically accessible surface area was compared using the double-layer capacitance (C_{dl}) extracted from non-faradaic scan-rate-dependent cyclic voltammetry (Fig. S11).[36] B–CoO_xS_y exhibits a higher C_{dl} (1.24 mF cm^{-2}) than CoO_xS_y (0.93 mF cm^{-2}) (Fig. 2d), consistent with a larger electrochemically accessible interface. This trend is consistent with the hierarchical, rough-surfaced, nano-subunit-assembled morphology observed by electron microscopy, which can increase electrolyte access and the density of electrochemically accessible sites. To compare intrinsic catalytic activity, we evaluated electrochemically active surface area (ECSA)-normalized linear sweep voltammetry (LSV) curves for the samples (Fig. S12). Durability was evaluated by 1000 continuous cyclic voltammetry cycles in 1.0 M KOH. The polarization curve

This journal is © The Royal Society of Chemistry 2026

Open Access Article. Published on 01 April 2026. Downloaded on 4/22/2026 1:27:01 PM.
This article is licensed under a Creative Commons Attribution-NonCommercial 3.0 Unported Licence.

after cycling nearly overlaps the initial curve with only a minor change at high potentials (Fig. S13), indicating stable OER performance under alkaline cycling. The post-OER Raman spectrum of B–CoO_xS_y retains the characteristic vibrational bands, indicating that local coordination and structure are largely preserved after OER (Fig. S14). Post-OER XPS of the cycled electrode (Fig. S15) suggests minor surface boron depletion after cycling, which may contribute to a small loss in activity. A performance comparison with representative related OER catalysts reported in alkaline media is provided in Table S3.

Density functional theory (DFT) calculations were performed to elucidate the structural and electronic origin of the enhanced OER activity observed upon boron incorporation. Two representative compositions were examined: an oxygen-incorporated model ($CoS_xO_{0.5}$) and a boron-doped model ($CoS_xO_{0.36}B_{0.2}$) (Fig. 3a and b). These formulas denote representative relaxed amorphous local-composition models selected from a series of structurally varied compositions to capture the experimentally indicated Co–S–O/B local chemistry, rather than exact stoichiometric phase assignments. Increasing oxygen incorporation into the disordered Co–S framework lowers the relaxed total energy of the models, consistent with stabilization of the oxygenated amorphous structure (Fig. S16 and Table S4). The stabilization is non-linear with oxygen content, indicating that compositional modification drives substantial electronic reorganization rather than a simple additive substitution effect. Oxygen incorporation also increases local distortion and disrupts long-range order, yielding highly disordered configurations in agreement with the experimentally observed amorphous character. Introducing boron into the oxygenated framework further lowers the relaxed total energy of the disordered models, consistent with additional stabilization of the oxygenated amorphous structure (Fig. S17 and Table S5). Because the compared models differ in composition, absolute energies should be interpreted cautiously. However, Bader charge analysis reveals clear trends in charge redistribution (Fig. 3c). In the oxygenated model, oxygen carries a substantial negative charge, consistent with polar metal-oxygen interactions in the disordered lattice. Upon boron incorporation, electron-deficient (Lewis-acidic) boron preferentially coordinates to lattice oxygen, forming strong, polar covalent $B^{\delta+}$–$O^{\delta-}$ interactions that reorganize the local bonding network. This B–O mediated redistribution reduces the net Bader charge depletion at Co (and S), indicating that Co retains higher electron density in the boron-containing sample (as also evidenced in the XPS analysis), and is consistent with enhanced Co d–O p hybridization (increased Co–O covalency). In turn, increased electron density at Co is expected to influence adsorption energetics and facilitate catalytic turnover. The initial adsorption of hydroxide (OH^-) to form surface *OH is a key early step in alkaline OER and is often rate-influencing. Therefore, OH^- adsorption energetics were evaluated at representative surface Co, S, lattice O, and B sites in the amorphous models. In both pristine and boron-containing frameworks, cobalt sites exhibit the most exothermic OH^- adsorption energies, supporting Co as the primary adsorption/activation center at the onset of OER. Structural relaxation following OH^- adsorption at Co sites reveals local coordination rearrangement and pronounced electron-density accumulation in the Co–O bond region, consistent with strong Co–*OH interaction (Fig. S18). Sulfur sites can also bind OH^-, but with less favorable energetics than cobalt, and their adsorption strength is only weakly perturbed by boron incorporation (Fig. S19). In contrast, adsorption on lattice oxygen sites is energetically unfavorable, consistent with electrostatic repulsion between negatively charged surface $O^{\delta-}$ species and incoming OH^- and suggesting that lattice oxygen is unlikely to be the dominant site for initial hydroxide uptake in this system (Fig. S20). Notably, boron incorporation introduces an additional thermodynamically accessible adsorption motif. The calculated OH^- binding at B sites is stronger than at S and lattice O sites, while remaining weaker than at Co, thereby increasing the number of energetically accessible hydroxylation/activation sites without displacing cobalt from its primary catalytic role (Fig. 3d and Fig. S21). Charge-density contour analysis further shows appreciable B–OH interaction accompanied by local structural relaxation, including reorientation of neighboring oxygen species and changes in the local O/S coordination environment (*e.g.*, altered nearby S–O connectivity), indicating enhanced local lattice adaptability during adsorbate accommodation (Fig. S21). Together, these results support a cooperative-site picture in which Co remains the principal redox-active center, while B functions as a secondary adsorption/activation site that can stabilize early hydroxylated intermediates (OH) and modulate the local reaction microenvironment. This interpretation is consistent with the electronic and chemical characterization. Bader charge analysis indicates that boron incorporation redistributes charge within the Co–O-S network, with reduced net

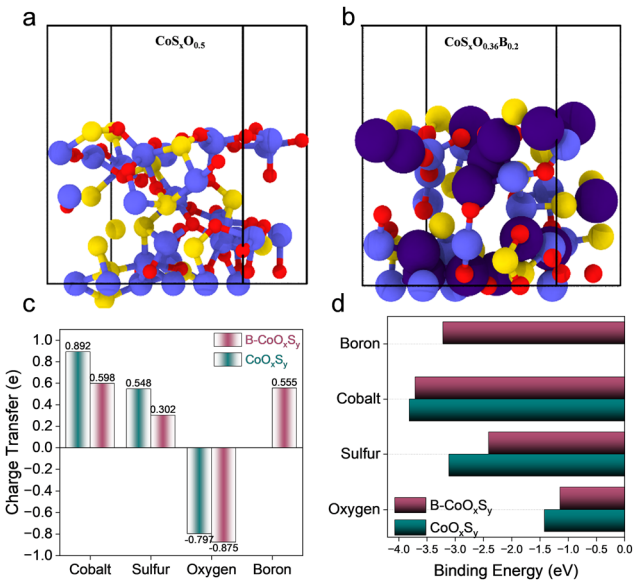

Fig. 3 (a) and (b) Relaxed amorphous models; (c) charge transfer as determined *via* Bader Charge Analysis (d) Comparison of the calculated binding energies of OH^- ions binding to various sites.

Open Access Article. Published on 01 April 2026. Downloaded on 4/22/2026 1:27:01 PM. This article is licensed under a Creative Commons Attribution-NonCommercial 3.0 Unported Licence.

charge depletion at Co (and S) and measurable boron participation in the local bonding environment *via* B–O interactions. In agreement, XPS shows a shift of the Co 2p features to lower binding energy and B 1s components assignable to B–O and B-metal environments, supporting chemical incorporation of boron and electronic coupling to the host framework. The increased electron density at Co, together with the calculated enhancement of Co d/O p hybridization near the Fermi level, provides an electronic basis for the modified OH^- adsorption response. Thus, boron incorporation offers a dual benefit, where Co remains the primary adsorption/activation center, while secondary B-centered OH^- adsorption motifs broaden the set of energetically accessible hydroxylation sites. Overall, the calculations suggest an adsorption hierarchy of Co–OH > B–OH > S–OH ≫ O–OH, and the reduced energy separation between Co and B sites provides a mechanistically consistent rationale for the enhanced OER activity. Electronic structure analysis (projected density of states, PDOS) further clarifies the origin of enhanced catalytic performance (Fig. S22 and S23). Both pristine and boron-containing models exhibit finite state density at the Fermi level (E_F), consistent with favorable electronic transport for electrocatalysis. Upon boron incorporation, the near-Fermi-level PDOS is redistributed more symmetrically with enhanced overlap between Co 3d and O 2p states, consistent with increased Co–O covalency. Although the direct contribution of boron p-orbitals is modest, boron perturbs the electronic structure sufficiently to broaden band dispersion and increase state density near the E_F. Consistent with this electronic modulation, ultraviolet photoelectron spectroscopy (UPS) shows a work-function decrease upon boron incorporation (Φ: 4.67 → 4.15 eV; $\Delta\Phi = -0.52$ eV; Fig. S24), indicating altered surface Fermi-level alignment relative to vacuum.[37,38] This shift is consistent with the reduced charge-transfer resistance observed by electrochemical impedance spectroscopy under OER-relevant polarization. Overall, in the oxygenated parent CoO_xS_y, oxygen incorporation stabilizes the disordered lattice and makes initial OH^- adsorption energetics more favorable. In the B-doped analogue, B–O interactions further redistribute charge, strengthen Co–O covalency, and introduce secondary OH^- adsorption motifs. Nonetheless, Co remains the dominant adsorption/activation center, and B acts as a cooperative secondary site. Together with the increased electrochemically accessible interface inferred from C_{dl}, these effects provide a consistent mechanistic basis for the observed enhancement in alkaline OER activity upon B-doping.

In summary, we demonstrate that Lewis-acidic boron incorporation into an amorphous mixed-anion CoO_xS_y substantially enhances alkaline OER activity. B–CoO_xS_y reaches 10 mA cm^{-2} at an overpotential of 189 mV in 1.0 M KOH (*vs.* 290 mV for CoO_xS_y), exhibits reduced R_{ct}, and maintains stable performance upon cycling. Spectroscopy, UPS (reduced work function), and DFT collectively support a mechanism in which B–O interactions redistribute charge, increase Co–O covalency, and introduce secondary OH^- adsorption motifs that cooperate with Co centers during early surface hydroxylation. The results highlight heteroatom-enabled electronic regulation as a practical strategy to activate amorphous mixed-anion frameworks for efficient OER.

Conflicts of interest

There are no conflicts to declare.

Data availability

The data supporting this article are included in the main article and its Supplementary Information (SI).

Supplementary information include: experimental procedures, characterization data, electrochemical measurements, post-OER analyses, DFT calculations, and literature benchmarking. See DOI: https://doi.org/10.1039/d6cc01259k.

Acknowledgements

STS acknowledges primary support from the U.S. Department of Energy under grant # DE-EE0010431. STS also acknowledges National Science Foundation (NSF) support for XPS acquisition (NSF/CHE 2216473) and partial support through the XLEAP award (NSF-BIO 2330043). AVK and ANN acknowledge the Dodson Graduate School grant (UTEP). NZ acknowledges the support from NSF CMMI-2302981.

References

1 T. E. Jones, D. Teschner and S. Piccinin, *Chem. Rev.*, 2024, **124**, 9136–9223.
2 A. N. Nair, M. Noufal, R. Jayan, G. Gutierrez, Y. Ge, M. M. Islam, J. A. Hernandez-Viezcas, V. Zade, S. Tripathi, V. Shutthanandan, C. V. Ramana and S. T. Sreenivasan, *Small*, 2022, **18**, 2202648.
3 S. Yagi, I. Yamada, H. Tsukasaki, A. Seno, M. Murakami, H. Fujii, H. Chen, N. Umezawa, H. Abe and N. Nishiyama, *Nat. Commun.*, 2015, **6**, 8249.
4 N. Attarzadeh, K. Haritha, P. G. Nalam, F. Sanchez, K. Saini, S. T. Sreenivasan, S. Tan, V. Shutthanandan, D. Das and C. Ramana, *ACS Appl. Mater. Interfaces*, 2025, **17**, 28038–28054.
5 A. V. Krishnan, K. Saini, L. G. Enriquez, C. Ramana and S. T. Sreenivasan, *Small*, 2025, **21**, e08245.
6 J. Li, *Nano-Micro Lett.*, 2022, **14**, 112.
7 H. Sun, X. Xu, G. Chen and Z. Shao, *Carbon Energy*, 2024, **6**, e595.
8 J. Liu, J. Nai, T. You, P. An, J. Zhang, G. Ma, X. Niu, C. Liang, S. Yang and L. Guo, *Small*, 2018, **14**, 1703514.
9 T. Li, T. Jing, D. Rao, X. Jia, Y. Zuo, Š. Kment and R. Zbořil, *J. Mater. Chem. A*, 2021, **9**, 12283–12290.
10 R. D. Smith, M. S. Prévot, R. D. Fagan, S. Trudel and C. P. Berlinguette, *J. Am. Chem. Soc.*, 2013, **135**, 11580–11586.
11 H. Liu, F.-X. Ma, C.-Y. Xu, L. Yang, Y. Du, P.-P. Wang, S. Yang and L. Zhen, *ACS Appl. Mater. Interfaces*, 2017, **9**, 11634–11641.
12 P. Cai, J. Huang, J. Chen and Z. Wen, *Angew. Chem.*, 2017, **129**, 4936–4939.
13 A. Suryawanshi, R. A. B. John, A. Bhide, S. Gupta, M. Spreitzer, R. Patel, R. Fernandes and N. Patel, *Energy Fuels*, 2024, **38**, 18965–18975.
14 M. Chen, Y. Xie, J.-X. Wu, H. Huang, J. Teng, D. Wang, Y. Fan, J.-J. Jiang, H.-P. Wang and C.-Y. Su, *J. Mater. Chem. A*, 2019, **7**, 10217–10224.
15 L. Tao, S. Theruvakkattil Sreenivasan and R. Shahsavari, *ACS Appl. Mater. Interfaces*, 2017, **9**, 989–998.
16 M. Du, J. Shi, Y. Shi, G. Zhang, Y. Yan, P. Geng, Z. Tian and H. Pang, *Chem. Sci.*, 2024, **15**, 9775–9783.
17 S. B. Kale, A. C. Lokhande, R. B. Pujari and C. D. Lokhande, *J. Colloid Interface Sci.*, 2018, **532**, 491–499.

 This journal is © The Royal Society of Chemistry 2026

Open Access Article. Published on 01 April 2026. Downloaded on 4/22/2026 1:27:01 PM.
This article is licensed under a Creative Commons Attribution-NonCommercial 3.0 Unported Licence.

18 M. Manuraj, V. V. Mohan, S. A. Aravindh, S. S. Kumar, K. N. Unni and R. Rakhi, *Chem. Eng. J.*, 2022, **443**, 136451.
19 R. Boppella, J. Tan, J. Yun, S. V. Manorama and J. Moon, *Coord. Chem. Rev.*, 2021, **427**, 213552.
20 C. Spori, L. J. Falling, M. Kroschel, C. Brand, A. Bonakdarpour, S. Kuhl, D. Berger, M. Gliech, T. E. Jones and D. P. Wilkinson, *ACS Appl. Mater. Interfaces*, 2021, **13**, 3748–3761.
21 C. Xuan, J. Wang, W. Xia, J. Zhu, Z. Peng, K. Xia, W. Xiao, H. L. Xin and D. Wang, *J. Mater. Chem. A*, 2018, **6**, 7062–7069.
22 Y. Yang, R. Wang, L. Yang, Y. Jiao and T. Ling, *Chem. Commun.*, 2020, **56**, 14154–14162.
23 A. Karmakar, A. V. Krishnan, R. Jayan, R. Madhu, M. M. Islam and S. Kundu, *J. Mater. Chem. A*, 2023, **11**, 10684–10698.
24 D. C. Cha, T. I. Singh, A. Maibam, T. H. Kim, D. H. Nam, R. Babarao and S. Lee, *Small*, 2023, **19**, 2301405.
25 F. Song, X. Ding, Y. Wan, T. Zhang, G. Yin, J. B. Brown and Y. Rao, *J. Phys. Chem. Lett.*, 2025, **16**, 3535–3543.
26 M. Yu, C. Weidenthaler, Y. Wang, E. Budiyanto, E. Onur Sahin, M. Chen, S. DeBeer, O. Rüdiger and H. Tüysüz, *Angew. Chem.*, 2022, **134**, e202211543.
27 S. Anantharaj, S. R. Ede, K. Sakthikumar, K. Karthick, S. Mishra and S. Kundu, *ACS Catal.*, 2016, **6**, 8069–8097.
28 M. Xiao, Q. Wu, R. Ku, L. Zhou, C. Long, J. Liang, A. Mavrič, L. Li, J. Zhu and M. Valant, *Nat. Commun.*, 2023, **14**, 5356.
29 W. Sun, Y. Wang, S. Liu, F. Lei, J. Xie and B. Tang, *Chem. Commun.*, 2022, **58**, 11981–11984.
30 Y. Huang, Z. Wang, S. Shen, L. Huang, W. Zhong, J. Pan and C. Li, *CrystEngComm*, 2022, **24**, 4857–4863.
31 A. Mariappan, P. Mannu, K. S. Ranjith, T. T. T. Nga, Y. K. Han, C. L. Dong, R. K. Dharman and T. H. Oh, *Small*, 2024, **20**, 2310112.
32 P. Wang, P. Wang, T. Wu, C. Zhao, Z. Pu and Y. Zhang, *Adv. Funct. Mater.*, 2025, **35**, 2417924.
33 P. Wang, Y. Luo, G. Zhang, Z. Chen, H. Ranganathan, S. Sun and Z. Shi, *Nano-Micro Lett.*, 2022, **14**, 120.
34 K. Zhang, G. Zhang, J. Qu and H. Liu, *Small*, 2018, **14**, 1802760.
35 Y. He, X.-P. Han, D.-W. Rao, Y.-D. Zhang, J. Zhao, C. Zhong, W.-B. Hu, W.-F. Wei and Y.-D. Deng, *Nano Energy*, 2019, **61**, 267–274.
36 A. N. Nair, M. F. Sanad, V. S. Chava and S. T. Sreenivasan, *Chem. Commun.*, 2022, **58**, 10368–10371.
37 Y. Lin, Y. Zhu, B. Zhang, Y. A. Kim, M. Endo and D. S. Su, *J. Mater. Chem. A*, 2015, **3**, 21805–21814.
38 D. Majchrzak, M. Rybak, R. Bartoszewicz, J. Plutnar, U. Ahsan, M. Grodzicki, D. Hommel, M. Birowska, Z. Sofer and R. Kudrawiec, *npj 2D Mater. Appl.*, 2025, **9**, 53.